Received: 14 December 2021 | Revised: 22 February 2022 | Accepted: 16 March 2022

DOI: 10.1111/jace.18460

Journal of the American Ceramic Society

SPECIAL ISSUE ARTICLE

On electron loss lowering at hematite photoelectrode interfaces

Karen C. Bedin[1] | **Ingrid Rodríguez-Gutiérrez**[1,2] | **Lizandra R. P. Peregrino**[1] | **Lionel Vayssieres**[3] | **Flavio L. Souza**[1,2,4]

[1]The National Nanotechnology Laboratory (LNNANO), Brazilian Center for Research in Energy and Materials (CNPEM), Campinas, Brazil

[2]Centro de Ciências Naturais e Humanas (CCNH), Federal University of ABC (UFABC), Santo André, Brazil

[3]International Research Center for Renewable Energy (IRCRE), State Key Laboratory of Multiphase Flow in Power Engineering, School of Energy and Power Engineering, Xi'an Jiaotong University, Xi'an, People's Republic of China

[4]Institute of Chemistry, University of Campinas (UNICAMP), Campinas, São Paulo, Brazil

Correspondence
Lionel Vayssieres, International Research Center for Renewable Energy (IRCRE), State Key Laboratory of Multiphase Flow in Power Engineering, School of Energy and Power Engineering, Xi'an Jiaotong University, Xi'an 710049, People's Republic of China.
Email: lionelv@xjtu.edu.cn
Flavio L. Souza, The National Nanotechnology Laboratory (LNNANO), Brazilian Center for Research in Energy and Materials (CNPEM), Campinas 13083-970, Brazil.
Email: flavio.souza@lnnano.cnpem.br

Funding information
CNPq, CAPES, and FAPESP, Grant/Award Numbers: 13/07296-2, 17/02317-2, 2021/07459-5; National Natural Science Foundation of China, Grant/Award Number: 2017/11986-5

Abstract

Photoelectrodes nanoscale interface design has become a key factor to enhancing their photoelectrochemical performance for water splitting by reducing the photogenerated charge recombination, thus ensuring their efficient separation, transport, and collection. In this work, hematite (α-Fe_2O_3) photoanodes were prepared from a simple and scalable methodology capable of synergistically mitigating the charge loss and recombination at all interfaces (i.e., fluorine-doped tin oxide/hematite, hematite/hematite, and hematite/electrolyte) and achieving overall efficiency of ~50% for the water oxidation reaction compared to pristine photoelectrodes. The external quantum efficiency at 1.23 V versus reversible hydrogen electrode of pristine hematite was enhanced 6.7 times with the modifications of the three interfaces (Al_2O_3/NbH/$NiFeO_x$). Electrochemical impedance spectroscopy and intensity-modulated photocurrent spectroscopies were applied to probe and monitor the photogenerated charge carrier dynamics revealing a substantial improvement in charge separation and collection at the back-contact interface as well as a partial mitigation of the surface states at the hematite–electrolyte interface.

KEYWORDS
energy conversion, hematite, interfaces, surface modification, thin films

1 | INTRODUCTION

Hematite is a very attractive candidate as a photoanode in photoelectrochemical (PEC) devices for low-cost and sustainable hydrogen production from solar water splitting. However, to achieve benchmark efficiency for commercial applications, several important issues must be addressed during its fabrication stage. Basically, the most relevant

drawbacks that need to be overcome are associated with interfacial recombination. At the solid–solid interface, for instance, the electrons (i.e., the majority carrier in n-type semiconductors) can be trapped at the grain–grain interface (or grain boundaries, GBs),[1] and they can also recombine or even be trapped at the substrate–hematite interface (i.e., the back-contact).[2] Assuming that the substrate choice is of central importance for designing hematite (α-Fe_2O_3) photoelectrode at the nanoscale, electrons can be lost directly from the substrate to the electrolyte, when hematite exhibits mesoporous morphology.[3,4] At the solid–liquid interface (hematite–electrolyte), the photogenerated holes (minority carrier) face a very short lifetime, diffusing only a few nanometers before recombining or being trapped due to the presence of surface states.[5–7]

Several approaches have been individually studied to mitigate the limiting processes at each interface summarized in various reviews,[8–10] such as the addition of cocatalysts and passivating agents at the solid/liquid interface,[11–14] the incorporation of modifying elements to change the bulk properties by doping or segregating[15,16] as well as thin interfacial layers,[17] often coated from atomic layer deposition, to improve the photocatalyst/substrate back contact.[18–24] Regardless of the interest and knowledge acquired about each individual interfaces, very little discussion can be found on the codependency between all these design modifications, mainly due to the complexity of the challenges facing the many different relevant pathways for charge losses within a photoelectrode.

It is also desirable that the photoelectrode design be based on a simple and scalable fabrication method, easily adaptable to the necessary modifications to reduce the photogenerated electron loss processes. Our group has been focusing on the understanding and experimental controls and developed new strategies to lower interfaces recombination in hematite photoanodes.[25,26] In particular, those prepared from polymeric precursor solutions have achieved benchmark values among the spin-coated ones in 2019.[27] Combining the experimental knowledge of the thermal treatment impact on commercial glass substrates,[28] as well as on the mechanical stress during the α-Fe_2O_3 phase formation and lattice mismatches at the back-contact,[29] we successfully engineered back-contact-rich interfaces between substrate and photocatalyst, minimizing interfacial and GB recombination by tailoring the polymeric precursor solution viscosity.[30]

Exploring the versatility of this approach and its adaptability to act in synergy with other potential modifications, herein, we strive to develop a versatile strategy to rationally engineer all relevant hematite photoanode interfaces using a simple chemical solution method. The synthetic route allows good thickness and stoichiometric controls, as well as the addition of elements and interface modifications. The three major interfaces are tailored by combining the coating of an Al_2O_3 underlayer, the addition of Nb ions, and the surface photoelectrodeposition of an $NiFeO_x$ cocatalyst, demonstrating how the design of an efficient photocatalyst is directly correlated with the lowering of electron losses at all the interfaces.

2 | EXPERIMENTAL DETAILS

Pristine and Nb-hematite thin films were designed following a chemical route optimized and adapted by our group to grow homogeneous layers over rough substrate surfaces with excellent coverage.[30] The thin films were prepared following strategically designed steps to mitigate the losses at the (1) hematite/substrate interface; (2) hematite/hematite grains interface; and at (3) hematite/electrolyte interface. The respective experimental steps were initiated by the substrate cleaning process and Al_2O_3 underlayer deposition, followed by the pristine hematite or Nb-hematite coating and the subsequent $NiFeO_x$ photoelectrodeposition as illustrated in Figure 1 and detailed in Sections 2.1–2.5.

2.1 | Substrate cleaning process

Aluminoborosilicate glass substrates coated with a fluorine-doped tin oxide (FTO, 10 Ω square^{-1}) on one side were purchased from Solaronix SA, with a physical area of 10.0 × 10.0 cm^2 and an overall thickness of 1.1 mm. Their transmission is higher than 80% in the 500–800-nm range and the average thickness of the FTO layer is ∼450 nm. For PEC sampling, they were used as 2.0 × 1.0 cm^2 substrates. The cleaning process followed three consecutive baths of 30 min each in boiling ultrapure water (18.2 MΩ cm at 25°C), absolute ethanol and acetone, both heated below their boiling points at 70 and 50°C, respectively.

2.2 | Al_2O_3 underlayer deposition

Aluminum acetylacetonate (Alfa Aesar) was used to prepare a 0.01-M solution in absolute ethanol (Merck, 99.5%) as a solution precursor source. The underlayers were coated onto a cleaned FTO substrate from 50.0 μL of the 0.01-M aluminum ethanolic solution by spin coating at 2000 rpm for 20 s, as illustrated in Figure 1, Step 1. This process was repeated twice and the substrates were then annealed in air at 300°C for 1 h.

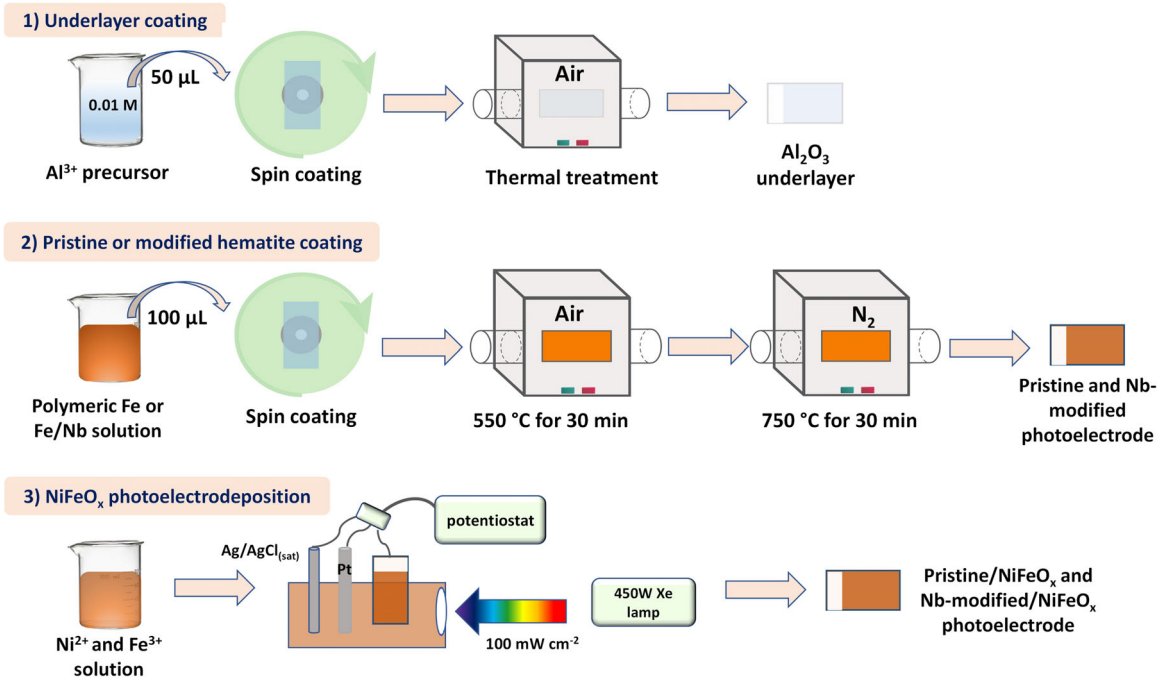

FIGURE 1 Scheme of the Al_2O_3 underlayer deposition and pristine and Nb-modified hematite thin films fabrication

2.3 | Hematite thin films preparation

Pristine hematite (Hem) and Nb-modified hematite (HNb) films were deposited onto the as-prepared Al_2O_3 underlayer from the polymeric precursor solution described in our recent work.[30] Briefly, the Fe^{3+} ions were chelated by citric acid in an aqueous media and, then ethylene glycol was added at 60–70°C to promote the polymerization. A 10.0-ml aliquot of this solution cooled to room temperature (25°C) was concentrated by heating it at ~70°C until a reduction of half of its volume, resulting in a pristine polymeric precursor.

The Nb-modified hematite polymeric precursor solution consisting of 0.60 ml of a 0.24-M $NbCl_5$ ethanolic solution was added in the 5.0-mL concentrated polymeric solution, stirred for 5 min for complete homogenization. After cooling down to 25°C, pristine and Nb-modified hematite precursor solutions were diluted with the addition of 1.50 ml of absolute ethanol (Merck, 99.5%) and 1.00 ml of isopropyl alcohol (Synth, 99.5%) and homogenized by stirring for 15 min. They were then stored in a refrigerator (T = 7°C) for 24 h before use. For the thin films preparation, the 25°C precursor solutions were subjected to agitation for proper homogenization. Then, 100 μl was spin coated (5 s at 500 rpm and 30 s at 7000 rpm) onto the Al_2O_3 underlayer, and the thin films were dried for 5 min at 90°C on a hot plate, followed by thermal treatments in air and N_2 atmosphere as detailed in Section 2.4.

2.4 | Thermal treatments

To eliminate organic compounds from the underlayer and hematite precursor solutions and crystallizing the metal oxide, the spin-coated films were subjected to a thermal treatment in air using a Lindberg/Blue M Mini-Mite™ horizontal tube furnace, model TF55035A. The furnace was preheated at the desired temperature, which was also verified by an external thermocouple at the central position of the ceramic tube where the sample will be located. For the treatments, the film was always placed in the center of a standard ceramic alumina container, with the glass side of the substrate rested on its wall, then introduced in the furnace. The as-prepared aluminum underlayer was treated at 300°C for 1 h, whereas the hematite-based films were annealed at 500°C for 30 min, as shown in Figure 1, Steps 1–2. To promote the thermal activation on the hematite films, a subsequent annealing in N_2 atmosphere was carried out in an automatic sliding quartz tube furnace (OTF-1200X-50-SL, MTI Corporation) preheated at 750°C. The quartz tube is equipped with a vacuum pump and a pressure gauge coupled with its closure caps. The ceramic container with the film was placed in a central position of the quartz tube, which was then sealed and submitted to three consecutive steps of evacuation/pressurization with N_2 gas. After the last pressurization, the N_2 flow (18-ml min^{-1}) was maintained and the sliding furnace was manually positioned to the sample location. The fast treatment lasted 30 min at 750°C and, then, the furnace was

moved to another side to leave its fan automatically positioned below the film to cool it quickly. Completing this process, the pristine or Nb-modified hematite films were removed from the furnace (final stage of Step 2).

2.5 | $NiFeO_x$ photoelectrodeposition

Photoelectrodeposition of $NiFeO_x$ onto the hematite-based films (Figure 1, Step 3) was carried out by immersing the films in a pH 5.3 aqueous solution consisting of 16.0-mM $NiSO_4{\cdot}6H_2O$ (Sigma Aldrich, 99.9%), 5.0-mM $Fe_2(SO_4)_3{\cdot}H_2O$ (Sigma Aldrich, 97%), and 0.1-M $NaCH_3COO{\cdot}3H_2O$ (Sigma Aldrich, 99%).[31] The electrochemical cell was composed by a commercial (Metrohm Autolab) $Ag/AgCl_{(sat)}$ and platinum electrodes as the reference and counter electrode, respectively, and the hematite-based film as the working electrode. Then, one linear sweep voltammogram was performed from 0.5 to 0.9 V versus Ag/AgCl, at a scan rate of 10 mV s^{-1}, under simulated sunlight illumination of 100 mW cm^{-2} (details given in Section 2.7). No additional treatment was employed for the $NiFeO_x$ as-prepared films.

2.6 | Characterization

Optical absorption spectra were recorded between 220 and 800 nm, using a Shimadzu UV–VIS–NIR spectrophotometer UV-3600 Plus equipped with an integrating sphere, using a sample holder for thin films. Surface morphology of the underlayers and the hematite films was investigated by scanning electron microscopy (SEM) using a Quanta™ FEG 650 (FEI Company) equipped with an ETD detector, at an accelerating voltage of 2 kV. Surface topography was examined by atomic force microscopy (AFM), NX-10 Park Systems, recording a scanning image area of $2.0 \times 2.0\ \mu m^2$ with a resolution of 512×512 pixels. The intermittent contact (tapping) mode was used, with silicon probe Nano World, FMR model, maintaining a resonance frequency of 75 kHz and force constant of 2.8 N m^{-1}. The root-mean-square roughness value of each film was calculated by the Gwyddion Software.

2.7 | (Photo)electrochemical experiments

All electrochemical and PEC experiments were performed in a three-electrode electrochemical cell, with a platinum electrode as the counter electrode, a commercial (Metrohm Autolab) $Ag/AgCl_{(sat)}$ electrode as the reference electrode, and the thin film as a working electrode with a fixed area. A potentiostat/galvanostat (Autolab PGSTAT129N) was used for all the experiments and the potentials were converted to the reversible hydrogen electrode (RHE) using the following Nernst equation:

$$E_{RHE} = E_{Ag/AgCl} + E^{\circ}_{Ag/AgCl} + 0.059 \times pH \quad (1)$$

For cyclic voltammetry measurements, the cleaned FTO substrate, Al_2O_3 underlayer, pristine, and modified hematite films were immersed in 1.0-M KOH containing 10-mM $K_4[Fe(CN)_6]$ electrolyte solution. Cyclic voltammograms (CVs) were recorded from 0.7 to 1.6 V versus RHE, using a scan rate of 10 mV s^{-1}. A 450-W Xe lamp (Osram, ozone free) equipped with an AM 1.5 global filter was used for the measurements under simulated sunlight illumination of 100 mW cm^{-2}. The linear sweep voltammetry, electrochemical impedance spectroscopy (EIS), and intensity-modulated photocurrent spectroscopy (IMPS) measurements were performed using the same three-electrode configuration cell and 1.0-M NaOH (pH 13.6) as the electrolyte solution.

The IMPS measurements were performed using a Metrohm Autolab PGSTAT302 N/FRA2 setup, utilizing a 470-nm high-intensity blue LED as an illumination source (DC intensity = 30 mW cm^{-2}). The experiments were performed applying a sinusoidal modulation on the light intensity with an amplitude of 10% of the base one, in the frequency range from 10 kHz to 0.01 Hz. The linearity of the response was tested and confirmed using Lissajous plots. The IMPS spectra were normalized by determining the number of modulated photons. The EIS measurements were performed from 10 kHz to 0.1 Hz and 10 mV without perturbation. An equivalent circuit was fitted to the experimental data, using the Z-View® software.

3 | RESULTS AND DISCUSSION

Figure 2 shows the AFM topographical and SEM images of the commercial FTO substrate, Al_2O_3 underlayer, pristine hematite, and Nb-modified hematite thin films deposited onto Al_2O_3. No pronounced differences can be noticed between the morphology of the pristine FTO (Figure 2A) and the one modified with the Al_2O_3 underlayer (Figure 2B), revealing the common irregular substrate surface. The pristine (Al_2O_3/H) and Nb-modified (Al_2O_3/NbH) hematite films showed the typical grain shape obtained from a polymeric precursor solution.[26,27] Surface roughness (RSM) value estimated from an AFM image was of 30 nm for the FTO and 29 nm for the underlayer, whereas the Al_2O_3/H and Al_2O_3/NbH thin films decreased to 10 and 6 nm, respectively. The goal behind Nb incorporation on hematite was to increase electron transport through the grains in the mesoporous morphology during the application. The more uniform

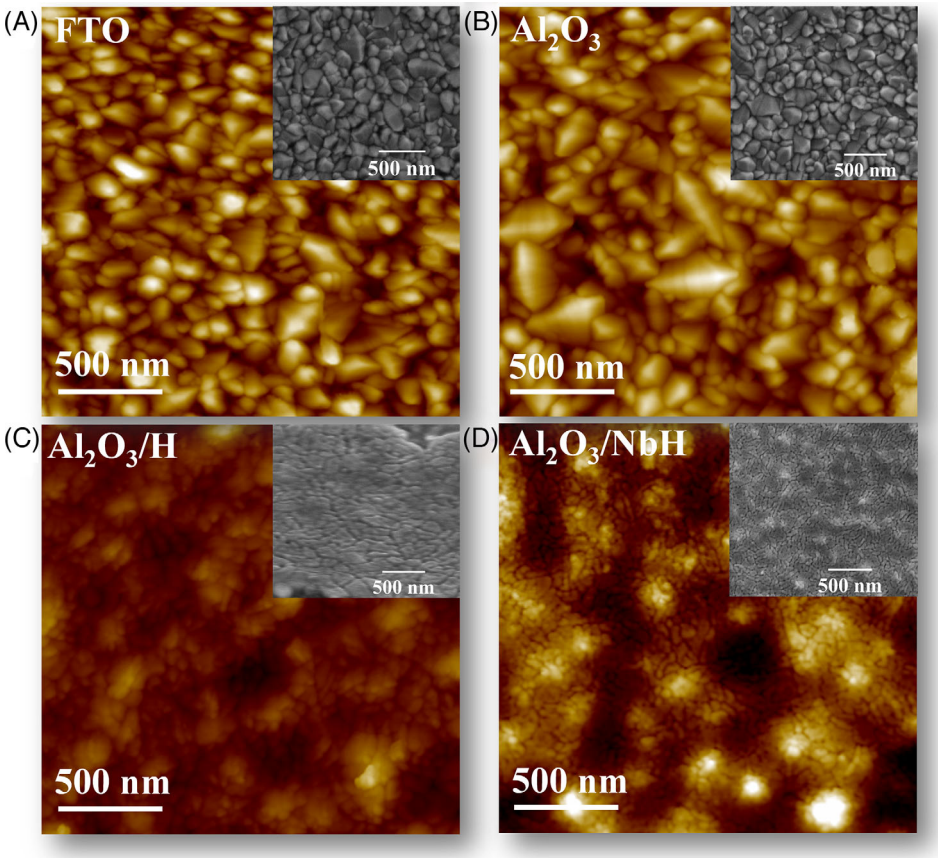

FIGURE 2 AFM topographical and SEM images of (A) commercial FTO substrate (FTO), (B) Al_2O_3 underlayer (Al_2O_3), (C) pristine hematite deposited onto Al_2O_3 (Al_2O_3/H), and (D) Nb-modified hematite deposited onto Al_2O_3 (Al_2O_3/NbH). AFM, atomic force microscopy; SEM, scanning electron microscopy. FTO, fluorine-doped tin oxide

Al_2O_3/NbH surface is the result of the segregation of the modifying element at the grain interfaces during the thermal treatment,[29,32] which arrangement was favored by the adopted methodology.[29] The species segregated act as pinning the grain growth,[33] as can be seen comparing Figure 2C and D, as well as contributing to a better accommodation of smaller NbH grains on the irregular substrate surface in relation to the hematite ones.

In addition, the average Al_2O_3/H thickness estimated from SEM cross-sectional image (not shown) was ~65 nm, whereas Al_2O_3/NbH thickness was reduced to about 50 nm due to its smaller average grain size. Both films presented similar absorbance spectra, as can be seen in Figure 3A. Indeed, only slight variations occurred in the hematite thin films deposited onto FTO and onto Al_2O_3 underlayer, mainly because there is no noticeable difference between FTO and Al_2O_3 spectra, as expected from the low precursor concentration used in the underlayer deposition and their transparent feature.

Although hematite thin films prepared from polymeric solution have a porous morphology that is beneficial for the charge transfer and surface reactions, it is worth keeping in mind that some FTO regions may still be exposed to the liquid electrolyte causing electron loss and short circuit. An insulating underlayer deposition, such as Al_2O_3, prior to the hematite thin film growth, could be a very effective way to prevent such issues.[22,23] To validate this assumption, dark CVs were performed with the commercial FTO, hematite film deposited on FTO (Hem), and Al_2O_3 underlayer (Al_2O_3/H) in a 10-mM $K_4[Fe(CN)_6]$ in a 1.0-M KOH electrolyte, as shown in Figure 3B.

As potassium hexacyanoferrate acts as an electron transfer mediator, a current response in its presence indicates a charge transfer between the working electrode and the electrolyte. Indeed, a pronounced current at 1.4–1.6 V versus RHE can be observed, besides a reversible broad peak at ~1.1 V versus RHE for the FTO, proving its propensity for transferring electrons directly to the electrolyte. Compared with the FTO, hematite thin films demonstrated a reduction of the anodic and cathodic stripping currents generated by the $Fe(CN)_6^{4-}/Fe(CN)_6^{3-}$ redox reactions, whereas the electron transfer was lower for Al_2O_3/H. Apparently, the Al_2O_3 underlayer helped to mitigate the transfer process, a role that can be observed in

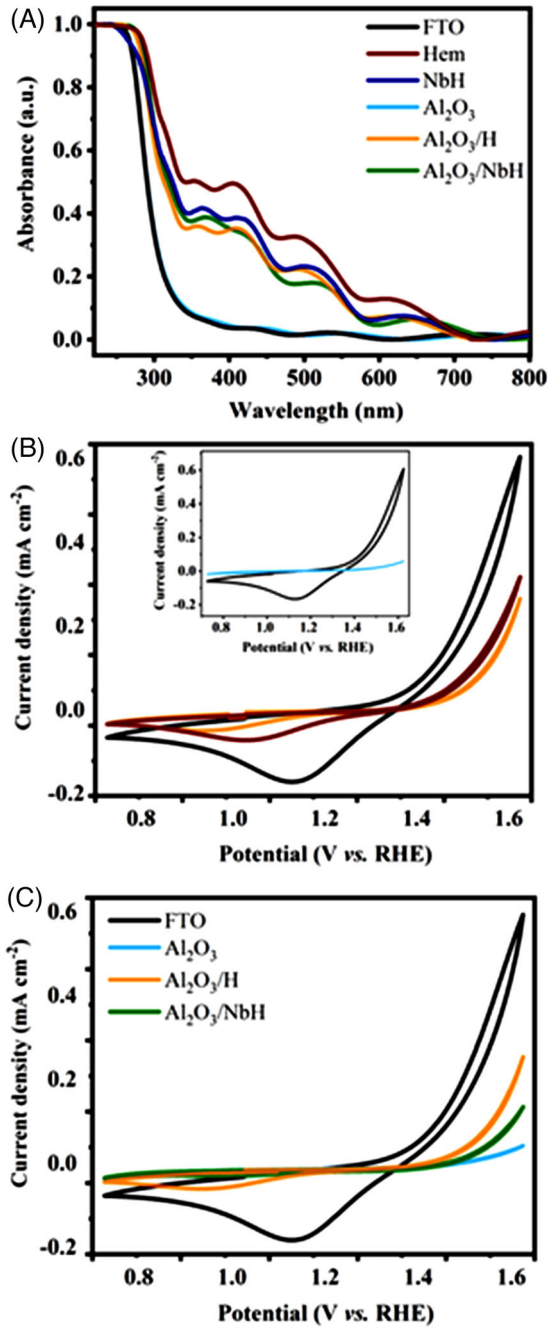

FIGURE 3 Optical absorbance spectra (A), dark cyclic voltammetry curves in 1.0-M KOH containing 10 mM $K_4[Fe(CN)_6]$ electrolyte solution for commercial FTO, Al_2O_3 underlayer, pristine hematite deposited onto FTO (Hem), pristine (Al_2O_3/H), and Nb-modified hematite (Al_2O_3/NbH) deposited onto Al_2O_3 (B and C), FTO, fluorine-doped tin oxide

the inset of Figure 3B, in which the linear curve evidences the Al_2O_3 blocking effect. This originates from its electrical insulation properties concomitantly with a uniform FTO coverage that prevents any area from being directly in contact with the electrolyte.[3] When comparing the CVs of pristine and Nb-modified hematite thin films with underlayer (Figure 3C), it can be noted that electron losses to the electrolyte are strongly avoided for Al_2O_3/NbH compared to Al_2O_3/H. The response of Al_2O_3/H may be due to the thermal treatment used in its preparation, in which the iron oxide phase is formed and there is a reconstruction of the grains on the substrate surface. Interactions between the iron, aluminum, and fluorine-doped tin oxide layers tend to occur in this process, which can result in areas of the FTO exposed.

The PEC response of all the pristine and Nb-modified hematite thin film samples was evaluated, together with an $NiFeO_x$ photoelectrodeposited onto them. Figure 4A shows the linear sweep voltammetry curves for hematite films in the absence of an underlayer, for which the main role of $NiFeO_x$ was as a cocatalyst, shifting the water oxidation onset potential. From the curves in Figure 4B, it can be noted that Al_2O_3/H and Al_2O_3/H/$NiFeO_x$ responses were similar to the analogous ones without an underlayer. As aforementioned, there is an interaction between the species during the thermal treatment that can promote Sn diffusion from FTO to hematite that has been associated with an enhancement of PEC activity.[34] The underlayer can avoid such diffusion, and a more accurate hematite activity is thus obtained. As no significant changes occurred in the Al_2O_3/H response in relation to pristine thin film (Hem), it can be inferred that there was no Sn diffusion from FTO to hematite, nor Al diffusion from the underlayer.

A moderate enhancement was obtained for Al_2O_3/NbH PEC response (Figure 4B) in relation to NbH (Figure 4A). It is important to emphasize that in both cases, the activity of hematite thin films modified with niobium was higher than those of pure hematite. Among all, the Al_2O_3/NbH/$NiFeO_x$ demonstrated a considerable improvement in photocurrent density for the entire reaction potential range, besides the cathodic shift of the onset potential. This result demonstrates the synergy between the underlayer and the Nb addition, as an indication that electron loss at the back contact is indeed suppressed, improving therefore the electron injection to the external circuit. Moreover, $NiFeO_x$ mostly acted to passivate the surface states as previously discussed in the literature.[32]

For a relevant comparison (and to avoid any misinterpretation), overall efficiency ($\eta_{overall}$) values were calculated from the ratio J/J_{abs}, in which J corresponds to the photocurrent measured at 1.23 V versus RHE and J_{abs} is the maximum photocurrent density obtained from the film absorbance efficiency. The corresponding results shown in Figure 4C clearly represent the improvement in efficiency with the Nb incorporation on hematite, related to its segregation during the thermal treatment that reduces grain sizes and increases the material area, as revealed by the AFM and SEM images. These changes demonstrated being

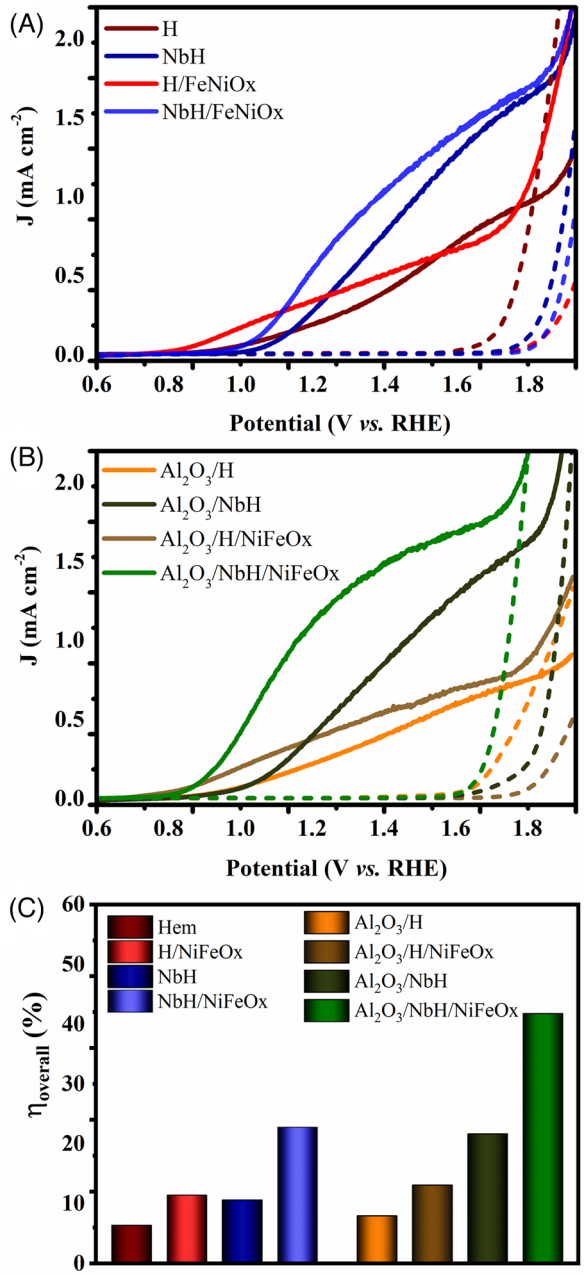

FIGURE 4 Linear sweep voltammetry for pristine and Nb-modified hematite thin films deposited onto FTO (A) and Al_2O_3 (B), with and without $NiFeO_x$ photoelectrodeposited in 1.0-M aqueous NaOH electrolyte under 100-mW cm^{-2} simulated sunlight illumination. Overall efficiencies ($\eta_{overall}$) calculated from the ratio J/J_{abs} (C). FTO, fluorine-doped tin oxide

efficient in promoting the charge separation and transport between hematite grains, culminating in a higher photoresponse. There were $\eta_{overall}$ enhancements of 1.7 times when comparing the NbH to the pristine Hem thin film and of 2.71 times for Al_2O_3/NbH related to the Al_2O_3/H, highlighting the importance of the underlayer on the performance.

$NiFeO_x$ is usually used as a cocatalyst, yet in this work it actually carried out a dual role, as a passivating agent for surface states as well as a cocatalyst, improving the photocurrent and shifting the onset potential, respectively. As previously discussed, its main role as a cocatalyst for the pristine hematite films resulted in an increased $\eta_{overall}$ of 1.8 and 1.6 times for the H/$NiFeO_x$ and Al_2O_3/H/$NiFeO_x$ thin films, whereas improvements of 2.1 and 1.9 times were obtained for the NbH/$NiFeO_x$ and Al_2O_3/NbH/$NiFeO_x$ samples. Interestingly, the degree of improvement obtained with the $NiFeO_x$ surface modifier was lower for the hematite films coated onto Al_2O_3 than those without the underlayer, which may be associated with electrons losses at the back contact, already resolved by the underlayer.

For a better comprehension of the individual as well as the synergic role of the modifications and to validate the effectiveness of our strategy, EIS and IMPS were carried out to analyze the photogenerated charge carrier dynamics. The EIS measurements were performed from 0.8 to 1.5 V versus RHE under illumination conditions (blue LED 470 nm, 30 mW cm^{-2}). Nyquist plots resulting from these measurements in aqueous NaOH electrolyte solution for Al_2O_3/NbH and Al_2O_3/NbH/$NiFeO_x$ are displayed in Figure 5A and E, respectively. In all cases, it can be noticed that the presence of two semicircles that are clearly influenced by the applied potential. For Al_2O_3/NbH (Figure 5A), the Nyquist plot shows a considerable impedance ($\boldsymbol{Z}$) dropping at $V > 1.10$ V versus RHE, which becomes even more significant at more positive potentials. Interestingly, after $NiFeO_x$ addition (Figure 5B), $\boldsymbol{Z}$ drops between 0.90 and 1.20 V versus RHE followed by a slight $\boldsymbol{Z}$ increase, which can be associated with the electrocatalytic effect of $NiFeO_x$ that affects the photocarrier kinetics.

In an effort to gain additional insight into the origin of these responses, EIS data of all samples were interpreted using an equivalent circuit model shown in the inset of Figure 5B. As previously reported,[32] the equivalent circuit elements include a space–charge capacitance of the bulk hematite, C_{bulk}, charge-transfer capacitance, C_{ct} associated with the surface states, whereas the resistances consist of series resistance, R_S, a resistance that represents the bulk resistance, R_{bulk} and a charge-transfer resistance from the electrode to the solution, R_{ct}. As a constant-phase element has been used to represent C_{ct}, its coefficient was calculated around 0.7–0.9 for better approximation to a conventional capacitor. Results from fitting the equivalent circuits to the impedance spectra described earlier can be found in Figure 5. In Figure 5B, it can be observed that R_{bulk} in hematite decreased with the presence of Al_2O_3 underlayer, but its drop is even more noteworthy when Nb is introduced in the synthesis. Moreover, the R_{ct} behavior

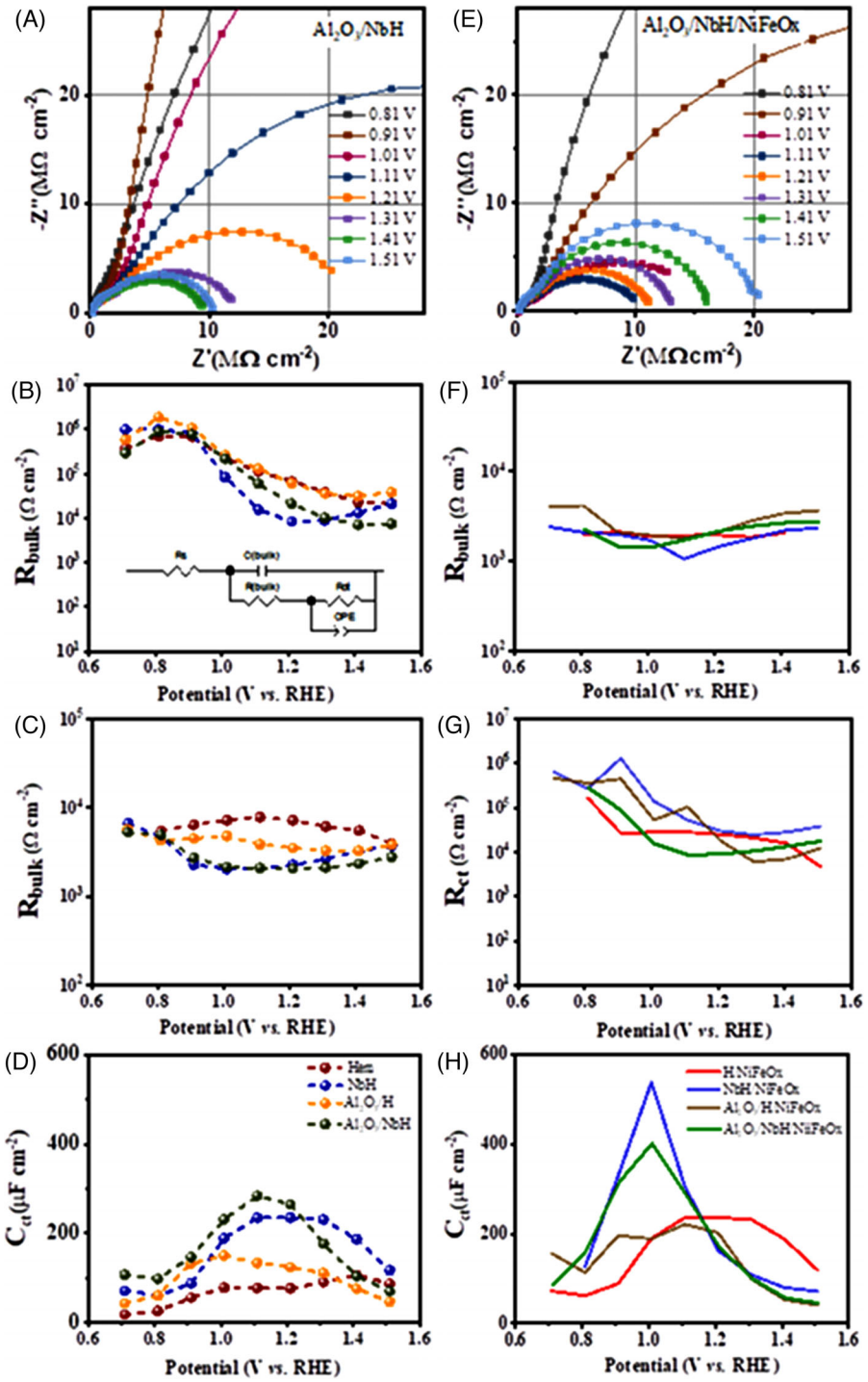

FIGURE 5 Nyquist plots for EIS data measured under 470-nm blue LED illumination (30 mW cm^{-2}) of (A) Al_2O_3/NbH and (E) Al_2O_3/NbH/$NiFeO_x$. Equivalent circuit parameters obtained from fitting EIS spectra of H, NbH, Al_2O_3/H, Al_2O_3/NbH before (B–D) and after (F–H) the addition of $NiFeO_x$ from 0.7 to 1.5 V versus RHE in 1-M NaOH electrolyte solution. The equivalent circuit used to deconvolute those parameters is displayed as an inset in (B). EIS, electrochemical impedance spectroscopy; RHE, reversible hydrogen electrode

(Figure 5C) also shows a decrease at $V > 0.9$ V versus RHE, arising its minimum values for NbH films. Further analysis of the C_{ct} shows a prominent peak for Al_2O_3/NbH and NbH samples that rises to their maximum at 1.10 and 1.20 V versus RHE, attributed to the charge accumulation of the surface states.[35] From the values obtained for C_{ct}, it can be concluded that a major quantity of holes successfully reach the surface when Nb is segregated on hematite thin films as the energy barrier at the grain–grain interface is lowered, as observed in previous reports for elements such as

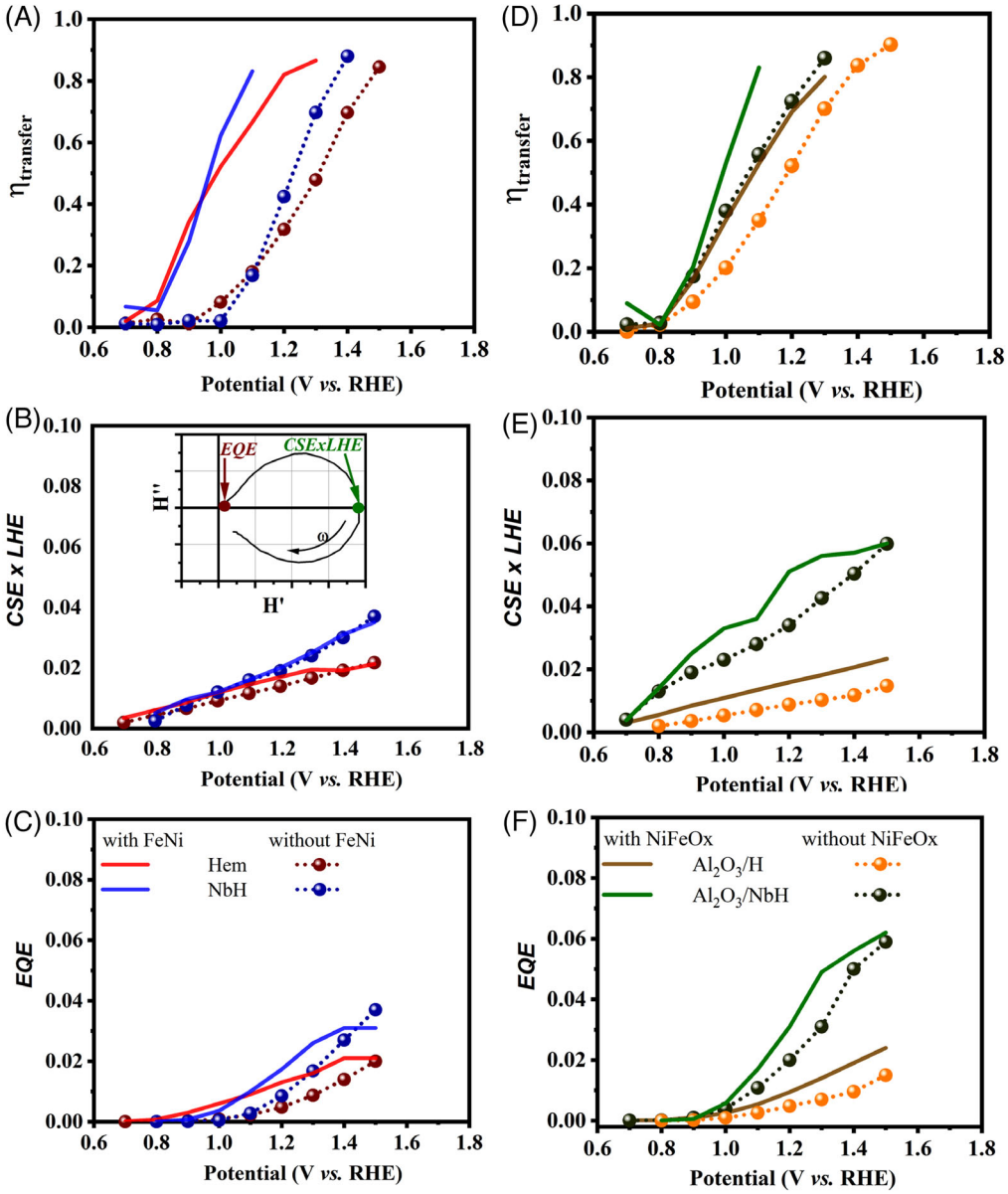

FIGURE 6 Relative transfer efficiency (h_{trans}), charge-transfer efficiency × light-harvesting efficiency (CSE × LHE), and EQE as a function of the applied potential obtained from IMPS plots for Hem, NbH (A–C) and Al_2O_3/H, Al_2O_3/NbH (D–F), in the absence and after $NiFeO_x$ deposition. EQE, external quantum efficiency; IMPS, intensity-modulated photocurrent spectroscopy. CSE, charge separation efficiency

Ti, Zr, and Sb.[36–38] Interestingly, the R_{ct} decrease observed at lower potentials compared to the C_{ct} peaks suggests that besides the number of holes available at the surface, the new surface states created by Nb require more energy to be activated, in agreement with the *J–V* curves.

After $NiFeO_x$ deposition (Figures 5F–H), the R_{bulk} dips for all samples, which indicates that the thickness (~50 nm) and the roughness of the films allow that $NiFeO_x$ not only acts at the surface but also somehow influences the bulk. A similar trend is observed for R_{ct} in which similar values are obtained for all samples. However, the most important variation is noticeable when the C_{ct} tendencies are analyzed: although the C_{ct} for hematite has been boosted, the C_{ct} of NbH samples are twice higher than the Hem and Al_2O_3/H films, confirming the major charge availability at the surface after Nb addition; furthermore, a cathodic shift on the C_{ct} peak after $NiFeO_x$ deposition in all samples shows the passivating effect of this electrodeposited compound.

IMPS, as a frequency-resolved optoelectronic characterization technique, was applied for elucidating the charge carrier dynamics in terms of charge separation efficiency (CSE), external quantum efficiency (EQE), and the kinetic constants of transfer (k_{tr}) and surface recombination (k_{sr})

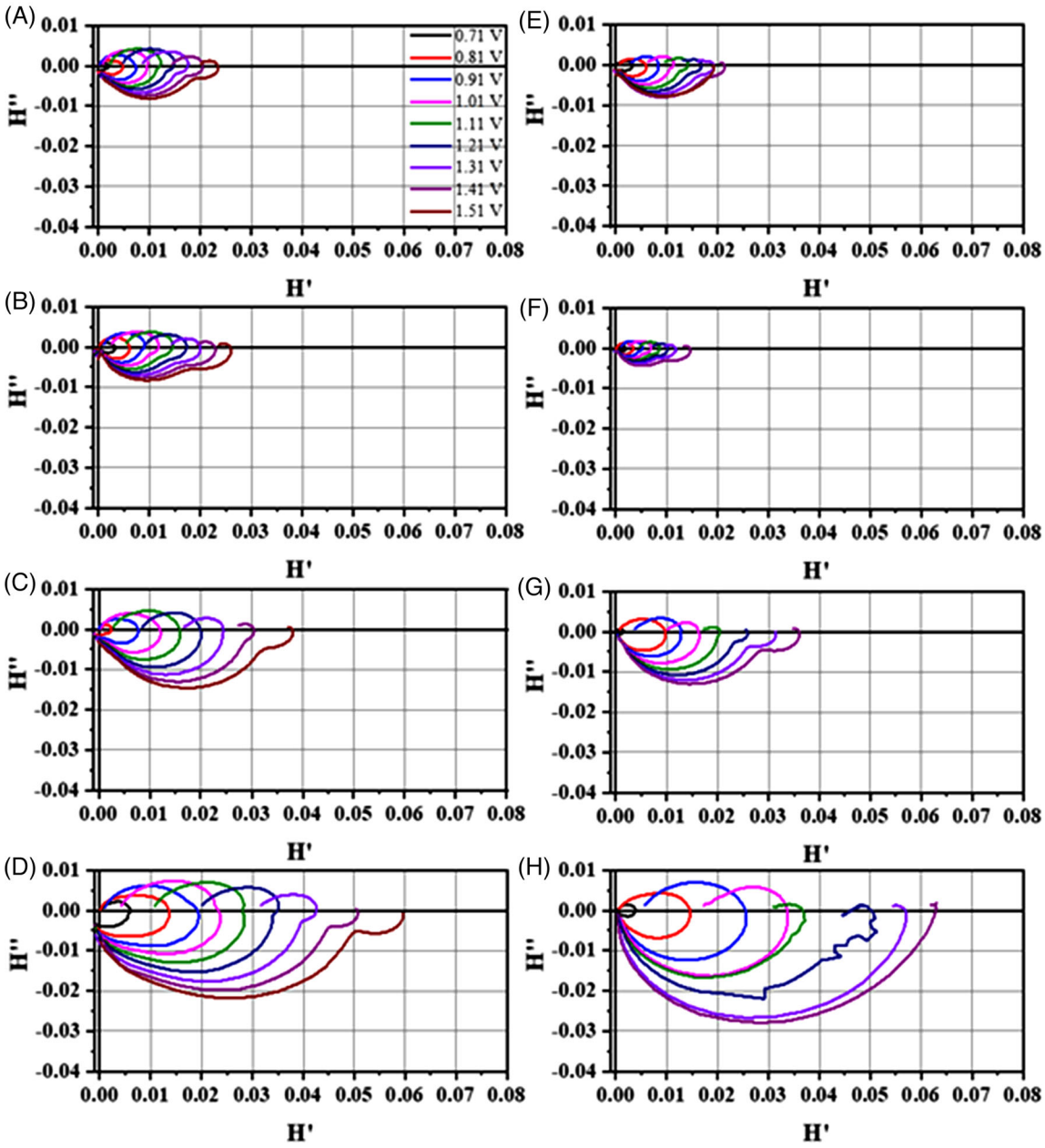

FIGURE 7 IMPS spectra obtained under blue LED illumination (30 mW cm^{-2}) for (A) pristine hematite (Hem) deposited onto FTO, (B) pristine hematite deposited onto Al_2O_3 (Al_2O_3/H), (C) Nb-modified hematite (NbH) deposited onto FTO, (D) Nb-modified hematite (Al_2O_3/NbH) deposited onto Al_2O_3 before $NiFeO_x$ deposition and the correspondent ones after $NiFeO_x$ deposition, (E) H/$NiFeO_x$, (F) Al_2O_3/H/$NiFeO_x$, (G) NbH/$NiFeO_x$, and (H) Al_2O_3/NbH/ $NiFeO_x$. IMPS, intensity-modulated photocurrent spectroscopy. FTO, fluorine-doped tin oxide

that are displayed in Figure 6. According to the IMPS theory,[39,40] the real axis (H') intercepts at medium frequencies is related to the CSE multiplied by the light-harvesting efficiency at a given wavelength (CSE × LHE), whereas the low-frequency intercept on H' can be defined as the EQE. Moreover, the high-frequency semicircle represents the charge transport and relaxation in the film, whereas the low-frequency semicircle is ascribed to the competition between the interfacial charge transfer and surface recombination.

From the IMPS spectra (Figure 7A and B), it can be noticed that for Hem and Al_2O_3/Hem, the spectra show the characteristic low-frequency loop that indicates that those samples face recombination problems due to surface states. For NbH and Al_2O_3/NbH (Figure 7C and D), this loop disappears at $V > 1.3$ V versus RHE, suggesting that

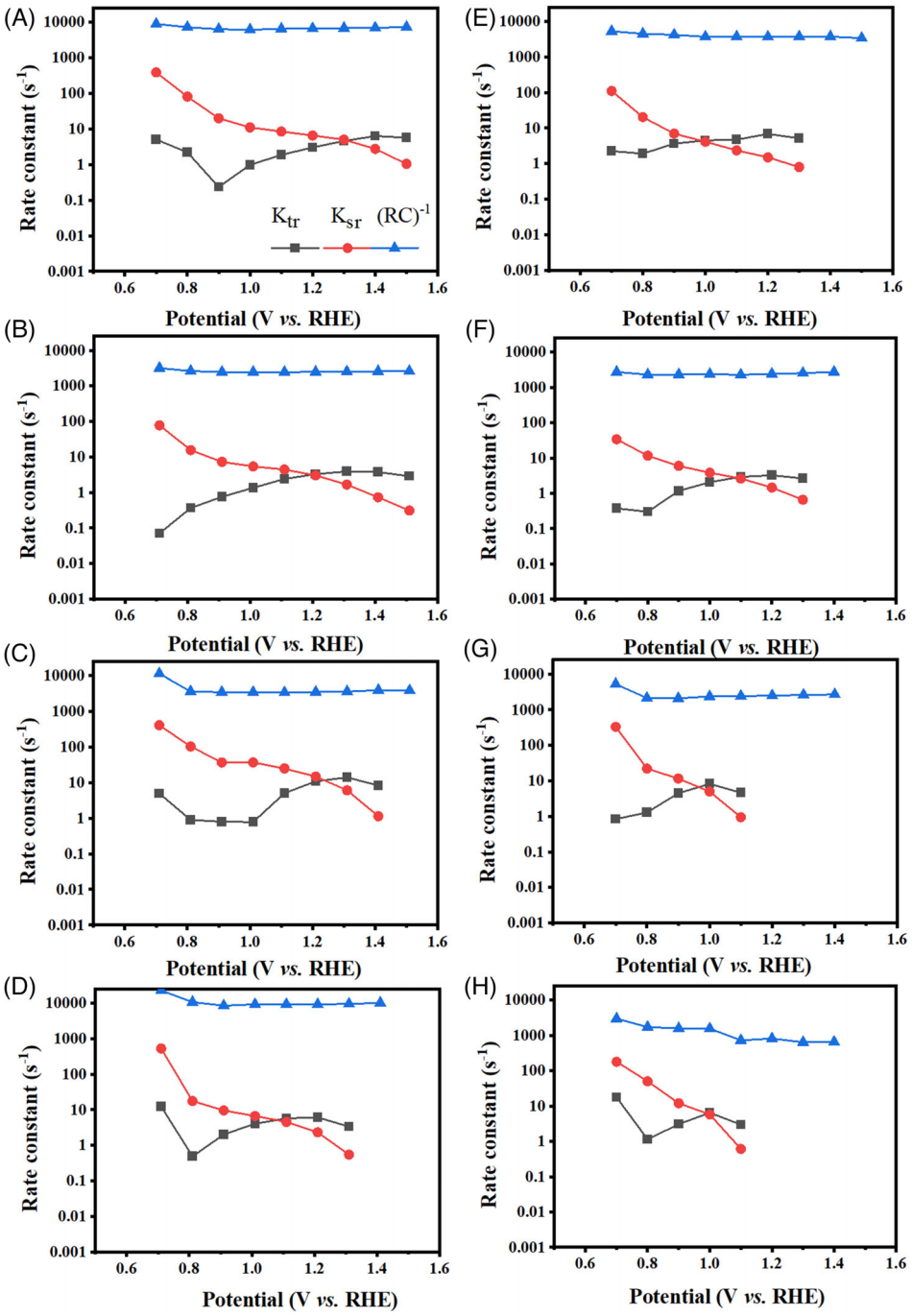

FIGURE 8 Charge-transfer rate constant (k_{tr}), surface recombination rate constant (k_{sr}), (E) and $(RC_{time})^{-1}$ cell constant obtained from IMPS spectra for (A) pristine hematite (Hem) deposited onto FTO, (B) pristine hematite deposited onto Al_2O_3 (Al_2O_3/H), (C) Nb-modified hematite (NbH) deposited onto FTO, (D) Nb-modified hematite (Al_2O_3/NbH) deposited onto Al_2O_3 before $NiFeO_x$ deposition and the correspondent ones after $NiFeO_x$ deposition, (E) H/$NiFeO_x$, (F) Al_2O_3/H/$NiFeO_x$, (G) NbH/$NiFeO_x$, and (H) Al_2O_3/NbH/$NiFeO_x$. IMPS, intensity-modulated photocurrent spectroscopy. FTO, fluorine-doped tin oxide

the surface states do not influence the photocurrent anymore. Furthermore, the IMPS Nyquist plots after $NiFeO_x$ deposition (Figure 7E–H) show that the abovementioned loop decreases significantly and tends to disappear at more negative potentials indicating that $NiFeO_x$ is somehow modifying the charge carrier kinetics, as also observed during the EIS analysis. Excitingly, at more positive potentials, all IMPS tend to form two semicircles at high frequencies at different relaxation times for each sample, which could indicate that the electron dynamics is being affected by the underlayer addition. Except for Al_2O_3/NbH/$NiFeO_x$ thin films, these processes are indistinguishable and,

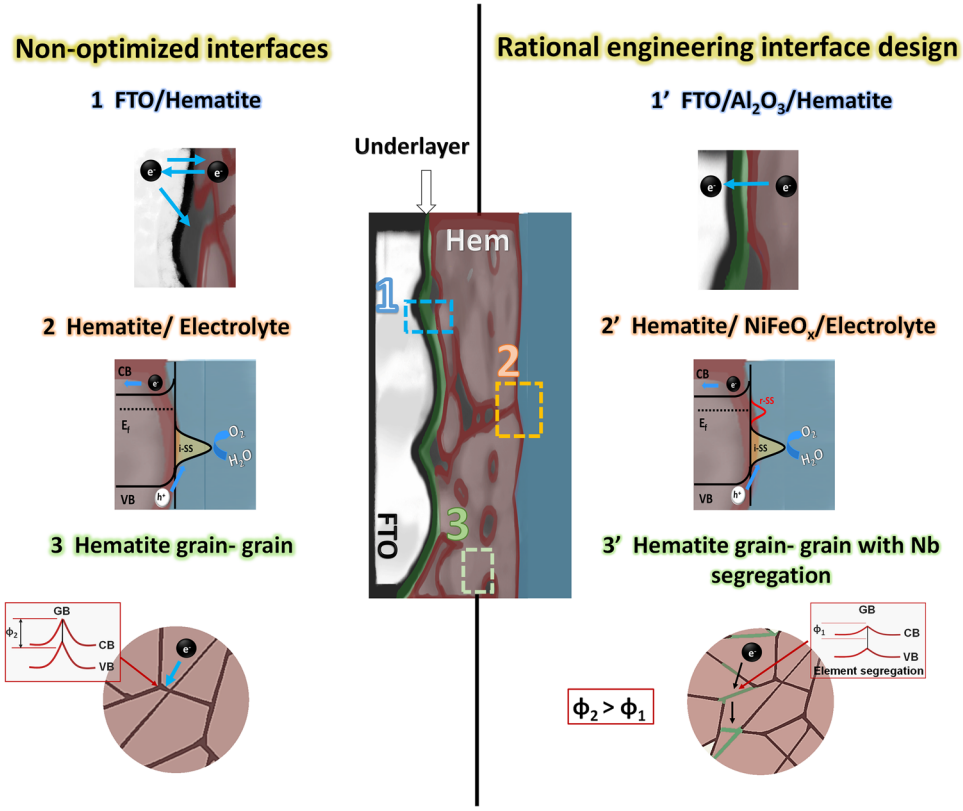

FIGURE 9 Scheme of the three modified interfaces addressed in this work: the electron losses taking place at the FTO/hematite (1, left) are mitigated by the Al_2O_3 (1′, right). The surface states (i-ss) present in the hematite/electrolyte interface were partially passivated (r-ss) by the inclusion of $NiFeO_x$ (2). The energy barrier associated with the hematite grain–hematite grain interface (ϕ_1) has been lowered by the Nb segregation (lighter lines on 3′). FTO, fluorine-doped tin oxide

as consequence, a distorted high-frequency loop is observed.

The recombination (k_{sr}) and transfer (k_{tr}) constants (Figure 8) have been obtained by deconvoluting them from the first quadrant semicircle relating the EQE, CSE × LHE, and the ω_{max} with the competition between surface recombination and hole transfer as reported elsewhere.[40] The crossing point between both constants (k_{sr} and k_{tr}) is consistent with the C_{ct} peak observed in EIS analysis confirming the significant influence of the surface states in the photoanode kinetics. Moreover, those constants were used to calculate the hole-transfer efficiency ($\eta_{transfer}$) defined as the ratio between the k_{tr} by the (k_{tr} + k_{sr}) displayed in Figure 6A and D. From these graphs, it can be noticed that the cathodic shift caused by $NiFeO_x$ is more significant in the absence of Al_2O_3 underlayer that indicates that the mitigation of electrons loss does improve holes transfer.

Analyzing the CSE × LHE and EQE values obtained from the intercepts as shown in the inset in Figure 6B and displayed in Figure 6B, C, E, and F, it can be noticed that $NiFeO_x$ is not modifying the CSE in the films, but it is modifying the hole injection to the electrolyte solution by passivating the surface states. By contrast, the Al_2O_3 underlayer is mainly enhancing the CSE as acting as a barrier layer for electron migration from FTO to hematite, which is also preventing the electron loss at the back-contact as observed for other underlayers.[41] Finally, IMPS analysis also confirms that Nb segregation in hematite strategy also enhances the CSE and EQE, but it is only noticeable at higher applied potential compared with bare hematite due to the new surface states possibly created by the Nb segregation at the hematite surface exposed to the aqueous electrolyte.

Our new design strategy applied for the overall design of hematite photoanodes is illustrated in Figure 9. As previously stated, three different approaches have been implemented to minimize the problems identified at the (1) FTO/hematite; (2) hematite/electrolyte; and (3) hematite grain/hematite grain interfaces. At the FTO/hematite interface (1′), the electron losses due to the existence of the electron traps or shunting recombination have been prevented by the presence of Al_2O_3 underlayer that acts as an active barrier for electron migration, hence, suppressing the electron back-injection from FTO to hematite. Moreover, the Nb addition in the precursor solution led to Nb segregation at some GBs (lighter lines

on 3′), which significantly enhances the low electron conduction at the hematite grain–hematite grain interface (3) by lowering the energy barrier (ϕ) and facilitating the electron migration through the grains to be collected at the FTO back-contact. Nb addition considerably improves the electron collection, its segregation also induces the formation of additional surface states (i-ss) associated with an anodic photocurrent onset shift and passivated (r-ss) by the subsequent electrodeposition of $NiFeO_x$ (2′) that avoids the surface recombination without altering the CSE.

4 | CONCLUSIONS

A novel rational strategy for the design of efficient hematite-based photoanodes was demonstrated with important implications for lowering electron loss at n-type photocatalyst based on a simple and low-cost methodology capable of mitigating synergically the interfacial photogenerated charge losses: at the FTO/hematite by the Al_2O_3 underlayer that enhances the electron injection to the back-contact; at the hematite grain–hematite grain (bulk) with Nb segregation that improves charge transport; and at the hematite/electrolyte by $NiFeO_x$ deposited that passivates surface states. These synergetic effects significantly increase the overall efficiency of hematite photoanodes for low-cost solar water-splitting and green hydrogen generation.

ACKNOWLEDGMENTS

The authors acknowledge CNPq, CAPES, and FAPESP (Grants Number: 13/07296-2 and 17/02317-2). F.L.S and K.C.B. acknowledge FAPESP (Grant Number: 17/11986-5 and 2021/07459-5) and Shell and the strategic importance of the support given by ANP (Brazil's National Oil, Natural Gas, and Biofuels Agency) through the R&D levy regulation. L.V. acknowledges the National Natural Science Foundation of China (NSFC) and the Outstanding Talent Program of Shaanxi Province as well as FAPESP (Grant Number: 2017/11986-5) and Shell and the strategic importance of the support given by ANP (Brazil's National Oil, Natural Gas, and Biofuels Agency) through the R&D levy regulation for financial support during his scientific visit to LNNANO/CNPEM in March 2020.

ORCID

Karen C. Bedin https://orcid.org/0000-0002-5086-7070
Ingrid Rodríguez-Gutiérrez https://orcid.org/0000-0001-6345-7321
Lizandra R. P. Peregrino https://orcid.org/0000-0003-3892-9854
Lionel Vayssieres https://orcid.org/0000-0001-5085-5806
Flavio L. Souza https://orcid.org/0000-0003-2036-9123

REFERENCES

1. Warren SC, Voïtchovsky K, Dotan H, Leroy CM, Cornuz M, Stellacci F, et al. Identifying champion nanostructures for solar water-splitting. Nat Mater. 2013;12(9):842–9.
2. Wang J, Feng B, Su J, Guo L. Enhanced bulk and interfacial charge transfer dynamics for efficient photoelectrochemical water splitting: the case of hematite nanorod arrays. ACS Appl Mater Interfaces. 2016;8(35):23143–50.
3. Shadabipour P, Hamann TW. Interface passivation to overcome shunting in semiconductor-catalyst junctions. Chem Commun. 2020;56:2570–3.
4. Kronawitter CX, Zegkinoglou I, Rogero C, Guo JH, Mao SS, Himpsel FJ, et al. On the interfacial electronic structure origin of efficiency enhancement in hematite photoanodes. J Phys Chem C. 2012;116(43):22780–5.
5. Li J, Chen H, Triana CA, Patzke GR. Hematite photoanodes for water oxidation: electronic transitions, carrier dynamics, and surface energetics. Angew Chem Int Ed. 2021;60(34):18380–96.
6. Zhang J, Cui J, Eslava S. Oxygen evolution catalysts at transition metal oxide photoanodes: their differing roles for solar water splitting. Adv Energy Mater. 2021;11(13):2003111.
7. Klahr B, Gimenez S, Fabregat-Santiago F, Hamann T, Bisquert J. Water oxidation at hematite photoelectrodes: the role of surface states. J Am Chem Soc. 2012;134:4294–302.
8. He Y, Hamann T, Wang D. Thin film photoelectrodes for solar water splitting. Chem Soc Rev. 2019;48:2182–215.
9. Steier L, Herraiz-Cardona I, Gimenez S, Fabregat-Santiago F, Bisquert J, Tilley SD, et al. Understanding the role of underlayers and overlayers in thin film hematite photoanodes. Adv Funct Mater. 2014;24(48):7681–8.
10. Laskowski FAL, Nellist MR, Qiu J, Boettcher SW. Metal oxide/(oxy)hydroxide overlayers as hole collectors and oxygen-evolution catalysts on water-splitting photoanodes. J Am Chem Soc. 2019;141(4):1394–405.
11. Kim JY, Youn DH, Kang K, Lee JS. Highly conformal deposition of an ultrathin FeOOH layer on a hematite nanostructure for efficient solar water splitting. Angew Chem Int Ed. 2016;55(36):10854–8.
12. Bedin KC, Muche DNF, Melo MA, Freitas ALM, Gonçalves R V., de Souza FL. Role of cocatalysts on hematite photoanodes in photoelectrocatalytic water splitting: challenges and future perspectives. ChemCatChem. 2020;12(12):3156–69.
13. Ding C, Shi J, Wang Z, Li C. Photoelectrocatalytic water splitting: significance of cocatalysts, electrolyte, and interfaces. ACS Catal. 2017;7(1):675–88.
14. Li D, Shi J, Li C. Transition-metal-based electrocatalysts as cocatalysts for photoelectrochemical water splitting: a mini review. Small. 2018;14(23):1–22.
15. Subramanian A, Gracia-Espino E, Annamalai A, Lee HH, Lee SY, Choi SH, et al. Effect of tetravalent dopants on hematite nanostructure for enhanced photoelectrochemical water splitting. Appl Surf Sci. 2018;427:1203–12.
16. Nogueira AE, Soares MRS, Junior JBS, Ramirez CAO, Souza FL, Leite ER. Discovering a selective semimetal element to increase hematite photoanode charge separation efficiency. J Mater Chem A. 2019;7(28):16992–8.
17. Ter Minassian-Saraga L, Vincent B, Adler M, Barraud A, Churaev NV, Eaton DF. et al. Thin films including layers: terminology in relation to their preparation and characterization.

IUPAC recommendations 1994. Thin Solid Films. 1996;277(1–2):7–78.
18. Hisatomi T, Dotan H, Stefik M, Sivula K, Rothschild A, Grätzel M, et al. Enhancement in the performance of ultrathin hematite photoanode for water splitting by an oxide underlayer. Adv Mater. 2012;24(20):2699–702.
19. Hisatomi T, Brillet J, Cornuz M, Formal Le F, Tétreault N, Sivula K, et al. A Ga_2O_3 underlayer as an isomorphic template for ultrathin hematite films toward efficient photoelectrochemical water splitting. Faraday Discuss. 2012;155:223–32.
20. Luo Z, Wang T, Zhang J, Li C, Li H, Gong J. Dendritic hematite nanoarray photoanode modified with a conformal titanium dioxide interlayer for effective charge collection. Angew Chem Int Ed. 2017;56:12878–82.
21. Zandi O, Hamann TW. Enhanced water splitting efficiency through selective surface state removal. J Phys Chem Lett. 2014;5:1522–6.
22. Hu Y, Boudoire F, Mayer MT, Yoon S, Graetzel M, Braun A. Function and electronic structure of the SnO_2 buffer layer between the α-Fe_2O_3 water oxidation photoelectrode and the transparent conducting oxide current collector. J Phys Chem C. 2021;125(17):9158–68.
23. Kay A, Cesar I, Grätzel M. New benchmark for water photooxidation by nanostructured α-Fe_2O_3 films. J Am Chem Soc. 2006;128(49):15714–21.
24. Kuroiwa K, Aoki T, Fujimoto M. Electrical properties of GaAs vapor phase epitaxial layers. J Cryst Growth. 1974;24:229–32.
25. Souza FL, Lopes KP, Nascente PAP, Leite ER. Nanostructured hematite thin films produced by spin-coating deposition solution: application in water splitting. Sol Energy Mater Sol Cells. 2009;93(3):362–8.
26. Bellido-Aguilar DA, Tofanello A, Souza FL, Furini LN, Constantino CJL. Effect of thermal treatment on solid-solid interface of hematite thin film synthesized by spin-coating deposition solution. Thin Solid Films. 2016;604:28–39.
27. Muche DNF, dos Santos TMG, Leite GP, Melo MA, Gonçalves R V., Souza FL. Tailoring hematite/FTO interfaces: new horizons for spin-coated hematite photoanodes targeting water splitting. Mater Lett. 2019;254:218–21.
28. Bedin KC, Freitas ALM, Tofanello A, Rodríguez-Gutiérrez I, Souza FL. Revealing the synergy of Sn insertion in hematite for next-generation solar water splitting nanoceramics. Int J Ceram Eng Sci. 2020;2(5):204–27.
29. Muche DNF, Carminati SA, Nogueira AF, Souza FL. Engineering interfacial modification on nanocrystalline hematite photoanodes: a close look into the efficiency parameters. Sol Energy Mater Sol Cells. 2020;208:110377.
30. Bedin KC, Mouriño B, Rodríguez-Gutiérrez I, Junior JBS, dos Santos GT, Bettini J. Solution chemistry back-contact FTO/hematite interface engineering for efficient photocatalytic water oxidation. Chin J Catal. 2022;42:1247–57 (Accepted Manuscript). https://doi.org/10.1016/S1872-2067(21)63973-6
31. Morales-Guio CG, Mayer MT, Yella A, David Tilley S, Grä M, Hu X. An optically transparent iron nickel oxide catalyst for solar water splitting. J Am Chem Soc. 2015;137:9927–36.
32. Freitas ALM, Muche DNF, Leite ER, Souza FL. Interface engineering of nanoceramic hematite photoelectrode for solar energy conversion. J Am Ceram Soc. 2020;103:6833–46.
33. Castro RHR. Interfacial energies in nanocrystalline complex oxides. Curr Opin Solid State Mater Sci. 2021;25(3):100911.
34. Ling Y, Li Y. Review of Sn-doped hematite nanostructures for photoelectrochemical water splitting. Part Part Syst Charact. 2014;31(11):1113–21.
35. Klahr B, Gimenez S, Fabregat-Santiago F, Bisquert J, Hamann TW. Electrochemical and photoelectrochemical investigation of water oxidation with hematite electrodes. Energy Environ Sci. 2012;5(6):7626–36.
36. de Lima FC, Schleder GR, Souza Junior JB, Souza FL, Destro FB, Miwa RH, et al. Unveiling the dopant segregation effect at hematite interfaces. Appl Phys Lett. 2021;118(20):201602.
37. Souza Junior JB, Souza FL, Vayssieres L, Varghese OK. On the relevance of understanding and controlling the locations of dopants in hematite photoanodes for low-cost water splitting. Appl Phys Lett. 2021;119(20):200501.
38. Rodriguez-Gutierrez I, Souza Junior JB, Leite ER, Vayssieres L, Souza FL. An intensity modulated photocurrent spectroscopy study of the role of titanium in thick hematite photoanodes. Appl Phys Lett. 2021;119(7):071602.
39. Rodríguez-Gutiérrez I, Djatoubai E, Rodríguez-Pérez M, Su J, Rodríguez-Gattorno G, Vayssieres L, et al. Photoelectrochemical water oxidation at FTO|WO_3@$CuWO_4$ and FTO|WO_3@$CuWO_4$|$BiVO_4$ heterojunction systems: an IMPS analysis. Electrochim Acta. 2019;308:317–27.
40. Rodríguez-Gutiérrez I, García-Rodríguez R, Rodríguez-Pérez M, Vega-Poot A, Rodríguez Gattorno G, Parkinson BA, et al. Charge transfer and recombination dynamics at inkjet-printed $CuBi_2O_4$ electrodes for photoelectrochemical water splitting. J Phys Chem C. 2018;122(48):27169–79.
41. Subramanian A, Annamalai A, Lee HH, Choi SH, Ryu J, Park, JH, et al. Trade-off between Zr passivation and Sn doping on hematite nanorod photoanodes for efficient solar water oxidation: effects of a ZrO_2 underlayer and FTO deformation. ACS Appl Mater Interfaces. 2016;8(30):19428–37.

How to cite this article: Bedin KC, Rodríguez-Gutiérrez I, Peregrino LRP, Vayssieres L, Souza FL. On electron loss lowering at hematite photoelectrode interfaces. J Am Ceram Soc. 2022;1–14. https://doi.org/10.1111/jace.18460